

Article

Dispensing Technology of 3D Printing Optical Lens with Its Applications

Fang-Ming Yu ^{1,*}, Ko-Wen Jwo ², Rong-Seng Chang ² and Chiung-Tang Tsai ²¹ Department of Electrical Engineering, St. John's University, New Taipei City 25135, Taiwan² Department of Optics and Photonics, National Central University, Taoyuan City 32001, Taiwan

* Correspondence: fmyu@mail.sju.edu.tw

Received: 15 June 2019; Accepted: 9 August 2019; Published: 14 August 2019



Abstract: Current 3D printed lens technology faces reduced efficiency due to stepped and stacked lens surfaces. This research employs a faster jet dispensing method which reduces these issues. It uses UV-curable material and merges droplets before they are cured to obtain very smooth lens surfaces without any post-processing and without manufacturing a mold for lens structures. This technology can be applied to lens manufacturing in a variety of products, especially in the form of arrays, saving development time and reducing cost. Two experiments of LED (Light-emitting diode) lens and solar cell lens array mask implementations are presented to demonstrate the power of the method. Furthermore, this study analyzes the effect of different contact angles created by jet dispensing technology, including a detailed exploration of fluid viscosity and tooling heating parameters. Our results show that the LED lens can be manufactured to increase the luminous flux of large angles. Furthermore, the lens array mask for solar cells can be manufactured to reduce sunlight reflection and increase secondary refraction, which enables solar cells to achieve higher photoelectric conversion efficiency and to increase their power generation up to 4.82%.

Keywords: photovoltaic module; low-reflection; structure of the surface

1. Introduction

In commonly seen 3D printing lens technology, the material is heated, melted, and squeezed through the nozzle to bond immediately with the previous layer of material (known as droplet injection technology). Layer upon layer of material is stacked [1,2] to form the lens surface. However, since droplet injection technology does not have a glue breaking mechanism, the disadvantage of this method is inconsistency [3,4]. Therefore, the aim of this research is to use a jet dispensing method to form lenses. The advantage of the jet valve is that it can provide a tiny dosage of fluid quickly and steadily, and it can adapt to different viscosities. This method is currently widely used in semiconductor packaging and assembly production for adhesive and underfill functions. Here, we made use of this jet valve feature to achieve rapid lens production and apply it in two sectors. The experiments were carried out at room temperature. Fast-curing UV fluids merge before curing, creating a very smooth lens surface; as such, no post-processing is required. The jet dispensing method has the advantage of reducing the required lens processing time by eliminating mold making. Lenses are created featuring diverse components, and effects can be quickly and easily fabricated and adjusted through integrations with different elements.

This study employed fluid viscosity and tooling heating parameters adjustments to study the effect of different contact angles during lens production. The final product shows that LED (Light-emitting diode) lenses created at a greater rotation angle will enhance the brightness of the lens and increase solar cell efficiency when the lens array is used in a solar collector.

2. Principle

2.1. Surface Tension

Surface tension is a physical effect, as shown in Figure 1. In the microscopic world, short-range attraction exists between molecules. Molecular attraction between the same kinds of molecules is known as cohesion. The attraction between liquid molecules is greater than the attraction of gas to gas molecules or liquid to gas molecules, so when the contact surface of a liquid and a gas cannot maintain a balanced state, the tensile force within the liquid propels the liquid surface into the smallest area possible. This makes the liquid surface look like it is covered with a layer of elastic film, which means that there is surface tension acting in the direction of the surface tangent.

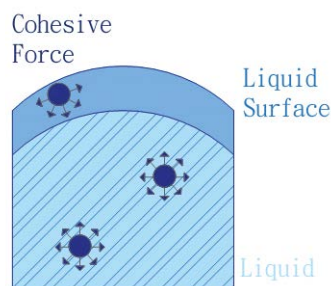


Figure 1. Schematic diagram of surface tension.

Surface tension refers to the applied force per unit length along the liquid surface; the formula can be written as:

$$\sigma = dF/dS \quad (1)$$

where σ is the surface tension, dF is the pulling force along the liquid surface vertical to dS , and dS is the unit length of the vertical tension.

According to the above equation, surface tension, in units of N/m, will rise as the temperature drops and vary with different contact surfaces. Surface tension decreases as size shrinks, and this main characteristic is often encountered in tiny devices. Figure 2 illustrates the comparative relationship between gravity and adhesion for various sizes of liquid surfaces. The figure clearly shows that when the length of the object is less than one millimeter, the effect of surface tension is greater than that of gravity, which means that liquids at this level become attached to the object because the adhesive force can resist the pull of gravity [5].

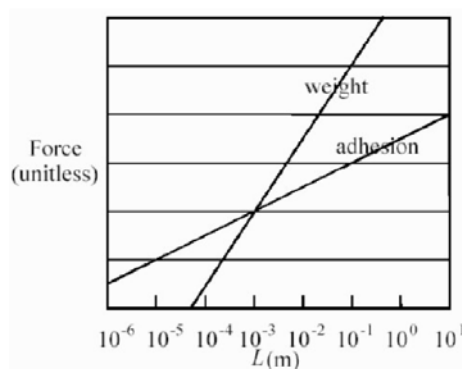


Figure 2. Scale relationship between gravity and molecular adhesion.

2.2. Contact Angle

In 1805, Thomas Young first proposed the concept of the contact angle [6]. As shown in Figure 3, when a droplet falls on an ideal flat surface, the droplet's peripheral line will be affected by three-phase

interfacial tension. When the forces are balanced, the angle θ_C between the solid surface and the tangent of the droplet is the so-called surface contact angle.

$$\gamma_{SG} - \gamma_{SL} = \gamma_{LG} \cos \theta_C \quad (2)$$

$$W = \cos \theta_C = \frac{\gamma_{SG} - \gamma_{SL}}{\gamma_{LG}} \quad (3)$$

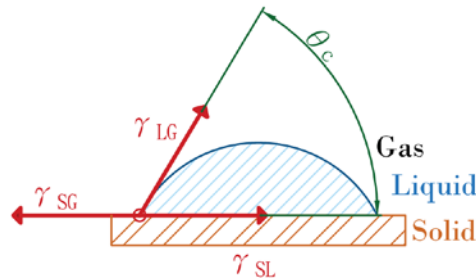


Figure 3. Contact angle diagram.

In the above equation, W is the wetting coefficient, γ_{SG} is the interfacial tension between the solid and the gas, γ_{SL} is the interfacial tension between the solid and the liquid, and γ_{LG} is the interfacial tension between the liquid and the gas.

In this experiment, we used an image measuring instrument to measure the width and height of the droplet in order to redraw the droplet using the multipoint extraction surface curve method, and output into a DXF (Drawing Exchange Format) file. We then used 3D drawing software to draw a line that passed through the three-phase point and was tangent to the droplet surface. The angle between this line and the droplet width was the contact angle used in this study.

2.3. Wettability

We use the term wettability to describe the physical state of a liquid on the surface of an object. It can be explained by the cohesive force between two molecules. The attraction between liquid molecules is called the cohesive force; the interaction between liquid molecules and surface molecules is called the adhesive force. The degree of wettability depends on the force balance of adhesion and cohesion. It involves three-phase materials including solid, liquid, and gas. Therefore, the process is closely related to thermodynamics. A change in energy for each interface leads to different behaviors, mainly divided into the following two kinds [7]:

2.3.1. Degree of Wetness

As shown in Figure 4, the droplets are hemispherical or elliptically attached to the surface and occupy a part of the surface volume on the solid surface. Since the adhesive force is greater here, the contact angle is less than 90° , which means that liquids have a higher wettability and will spread on the surface.

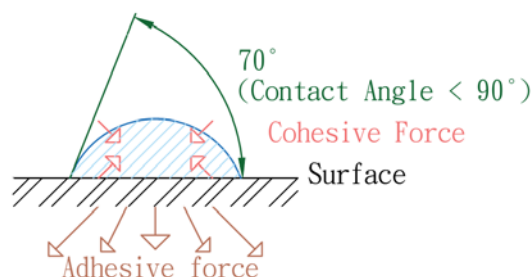


Figure 4. Degree of wetness diagram.

2.3.2. Low Wettability

As shown in Figure 5, the droplets attached to the surface are spherical. Since the adhesive force is smaller here, the contact angle is greater than 90° , which means that liquids have a lower wettability with a smaller contact area.

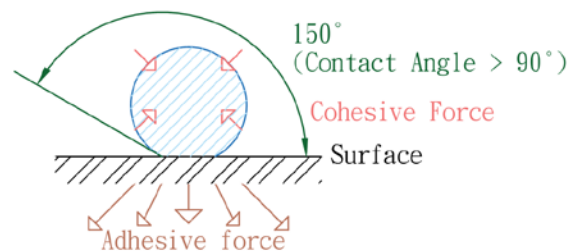


Figure 5. Low wettability diagram.

In Figure 6, UV fluids with different viscosities between CP2000 (CP: Centipoise, viscosity unit) and CP15000 are used to change the cohesive force, which in turn controls the contact angle $\theta_c(^{\circ})$ of the fluid on the slide in order to change the contact angle of its lens.

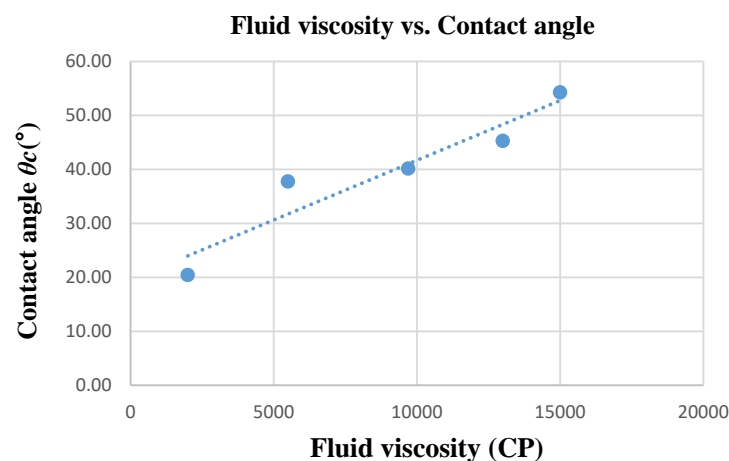


Figure 6. Relationship between fluid viscosity and contact angle θ_c .

In Figure 7, using a fluid with CP2000 viscosity and the same valve parameters, the fluid is dispensed onto a slide where the tool carrying it is heated from 25 to 75°C to adjust for the way different temperatures can change fluid cohesion.

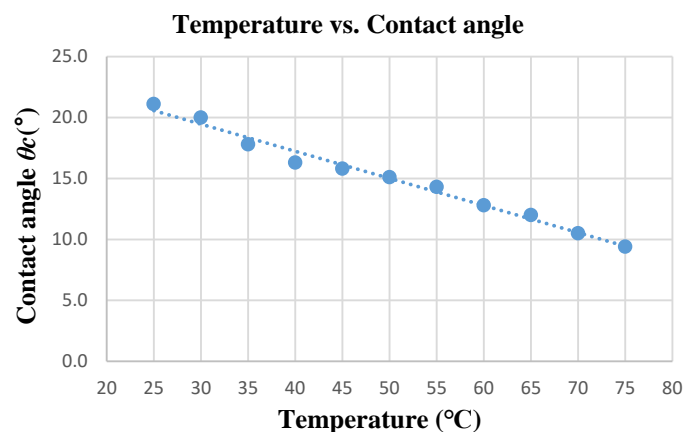


Figure 7. Relationship between tooling temperature and contact angle θ_c .

Linear regression, as seen in the above diagram, was used to draw the trend line and find the equation below. The relationship between the fluid with tooling temperatures at 25–75 °C and the contact angle is as follows:

$$\theta_C = -0.2225 \times T + 26.136 \quad (4)$$

where θ_C is the contact angle and T is the tooling temperature.

3. Equipment and Methods

3.1. Dispensing System

The Asymtec Axiom X-1020 [8] dispensing system model (Asymtec, Carlsbad, CA, USA) was used in this work, as shown in Figure 8. The dispensing system is commonly used in semiconductor mass production. It is suitable for bottom filling, gun filling, wafer bonding, and sealing. The system can achieve results high in precision and repeatability, and it is therefore suitable for mass production. It is widely applied to a variety of adhesive materials, production technologies and substrates used in the semiconductor packaging and assembly process [8,9].



Figure 8. Asymtec Axiom X-1020 dispensing system.

3.2. Jet Valve

Figure 9 depicts the jet valve, which is normally closed and uses a reflexive mechanism that is driven by compressed air. It uses the momentum conversion principle to squeeze out a precise amount of fluids. A high speed cylindrical coil used to adjust the compressed air acts on the base of the needle assembly. The liquid flows through the base after entering the adhesive tank. When air is exhausted, the needle moves rapidly to the closed position and dispenses the fluid through the nozzle to eject droplets. The continuous flow of droplets can be dispensed in a large volume or according to a specific shape.



Figure 9. Jet valve for dispensing.

3.3. Description of Experimental Process

The flow chart in Figure 10 shows the planning, process, and execution of the two experiments conducted in this research. It shows that the preprocess was the same for both, and the application of the technology was tested in two different ways.

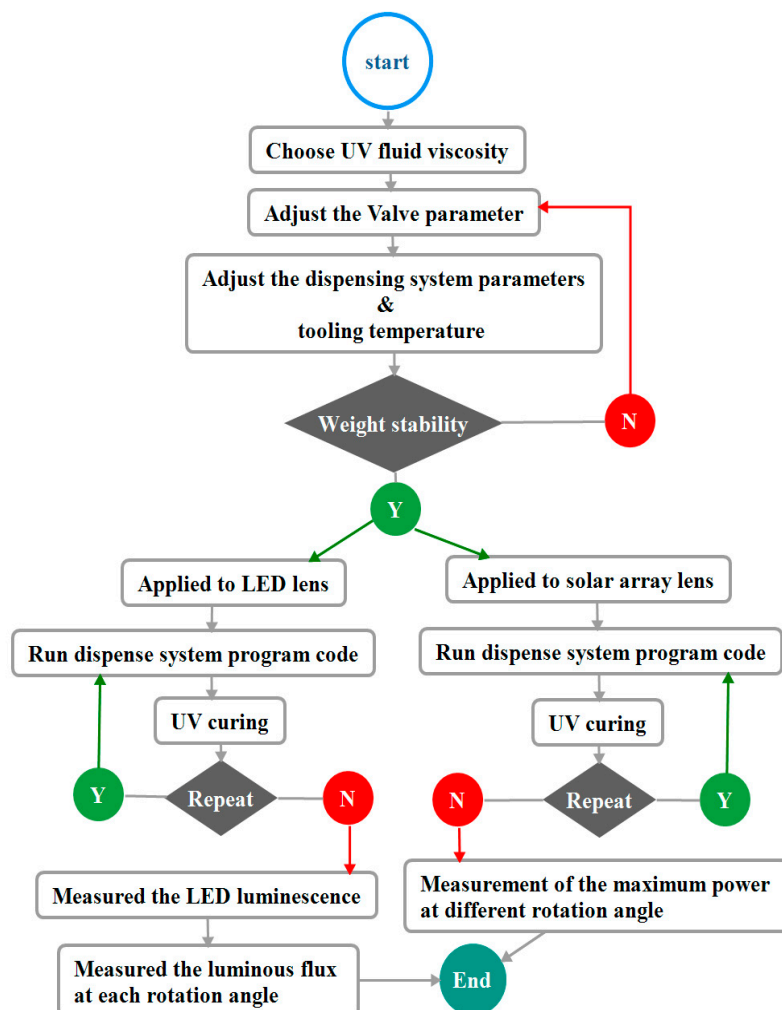


Figure 10. Experiment preprocess and execution flow chart.

3.4. Weight Stability

Before either experiment could be conducted, a weight stability experiment was necessary. This was due to the various possible combinations of the jet valve and the applicability of the fluid. As the name of the experiment implies, we set all jet valve parameters and specified the number of points where the fluid was dispensed into a cup. After weighing, the weight had to be divided by the number of points so that the weight of every single point could be obtained. This was repeated 50 times to acquire 50 pieces of data.

$$\text{Average } \bar{X} = \frac{1}{N} \sum_{i=1}^N X_i \quad (5)$$

Using the above formula, where N is 50 times, you can find the average weight of the experiment:

$$\text{Difference}(\%) = \frac{X_i - \bar{X}}{\bar{X}} \times 100\% \quad (6)$$

To determine the combination of the jet valve and its parameters in order to dispense fluids steadily, the error rate of each single point weight—which was calculated based on the formula above—should not have exceeded $\pm 5\%$, as shown in Figures 11–15. One factor we were trying to avoid was the surface of the lens becoming stepped, because power would become lost. Comparing Figures 11–15, we can see that the lower the viscosity, the higher the weight stability; additionally, the surface of the lens was less stepped. Figure 15 reflects results occurring after we heated the nozzle head to increase the weight stability, but, as predicted, the higher viscosity caused an increase in the stepped surface.

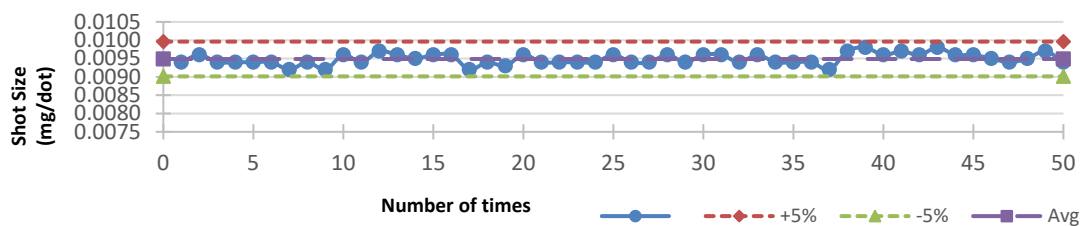


Figure 11. CP2000 (CP: Centipoise) viscosity UV fluid weight stability (USL (Upper Specification Limit): +5%, LSL (Lower Specification Limit): -5%, Target: Average).

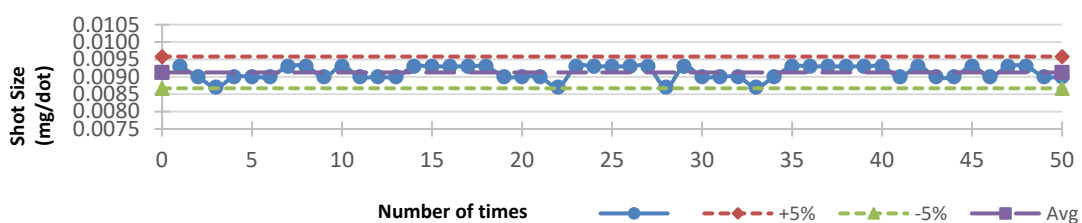


Figure 12. CP5500 viscosity UV fluid weight stability (USL: +5%, LSL: -5%, Target: Average).

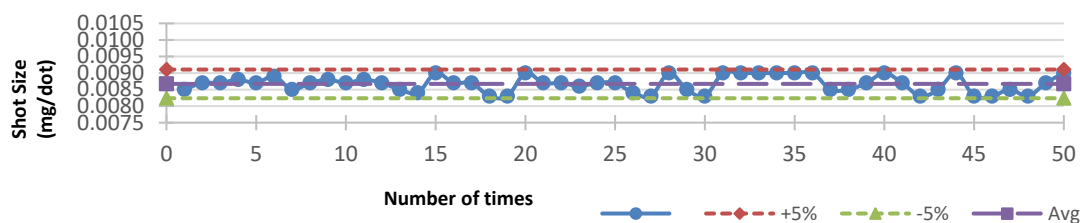


Figure 13. CP9700 viscosity UV fluid weight stability (USL: +5%, LSL: -5%, Target: Average).

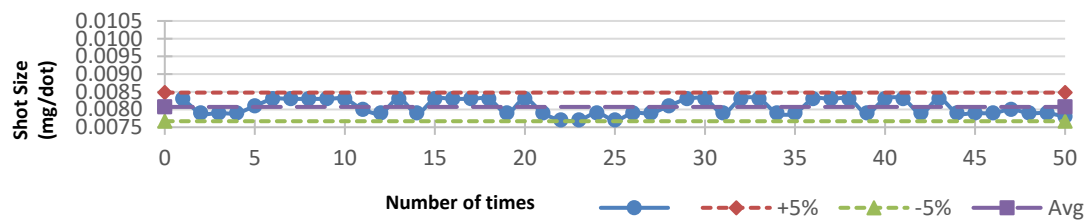


Figure 14. CP13000 viscosity UV fluid weight stability (USL: +5%, LSL: −5%, Target: Average).

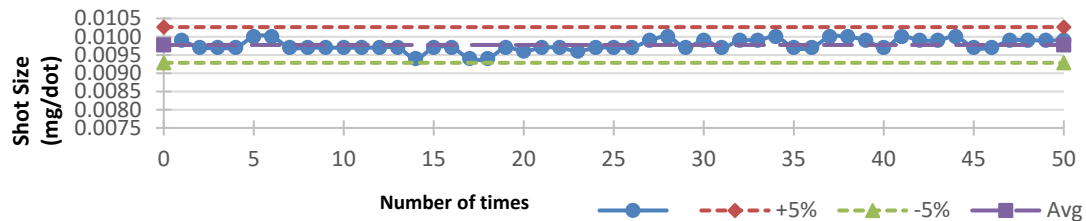


Figure 15. CP15000 viscosity UV fluid weight stability (USL: +5%, LSL: −5%, Target: Average).

4. Lens Production Experiment Results

4.1. Applied to LED Lens

UV fluid with CP2000 viscosity was dispensed onto the surface of a packaged LED product, where the tooling temperature was set at 30 °C. We used this kind of CP2000 viscosity fluid because it has a low viscosity, a high weight stability, and the stepped surface is not obvious. The dispensed fluid was stacked, layer upon layer, to increase its lens height, as shown in Figure 16. However, from Figure 16, we can see that not only was the height increased, but the contact angle was also greatly increased. After curing, an image measuring instrument was used to observe its surface contact angle $\theta_C(^{\circ})$; an UPRtek MK350N handheld spectrometer (UPRtek, Miaoli, Taiwan) was used to measure the effect of UV fluid on LED luminescence, as shown in Table 1. The MK350N spectrometer possesses the measuring capabilities of illuminance (LUX)/foot candle (fc), correlated color temperature (CCT), CIE chromaticity coordinates, and color rendering index (CRI, Ra) measurements. Most pertinent to this research, this spectrometer's BIN ranking features, with classifying the chromaticity of LED and making uniform BIN types, allow for fast CIE 1931 inspection and the confirmation of LED quality. In Table 1, from the CIE and CCT value, we can see the thicker LED lens layers produced more blue light, while the illuminance value was lower. Finally, the luminous flux of each LED lens rotation angle in layers 1–3 was measured (shown in Figure 17) to draw a luminous flux vs LED lens rotation angle diagram [10] (shown in Figure 18). Figure 17a,b is the schematic diagram and the actual tools used in the measurement system of luminous flux vs LED lens rotation angle. The measurements were taken by rotating the LED lens to obtain the luminous flux from the detector.

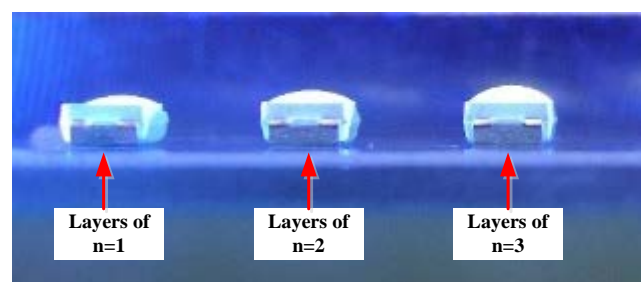


Figure 16. Jet dispensing applied on LED (Light-emitting diode) lens.

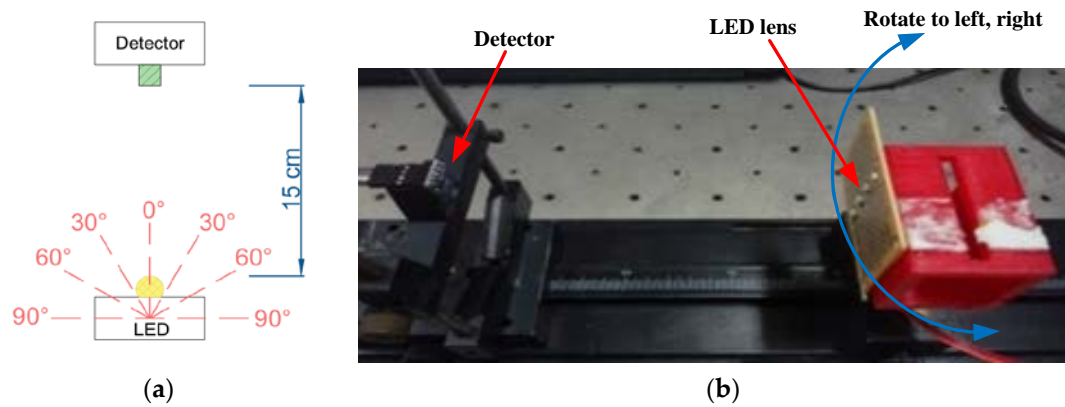


Figure 17. (a) The schematic diagram of luminous flux vs LED lens rotation angle measurement. (b) The actual system of luminous flux vs LED lens rotation angle measurement.

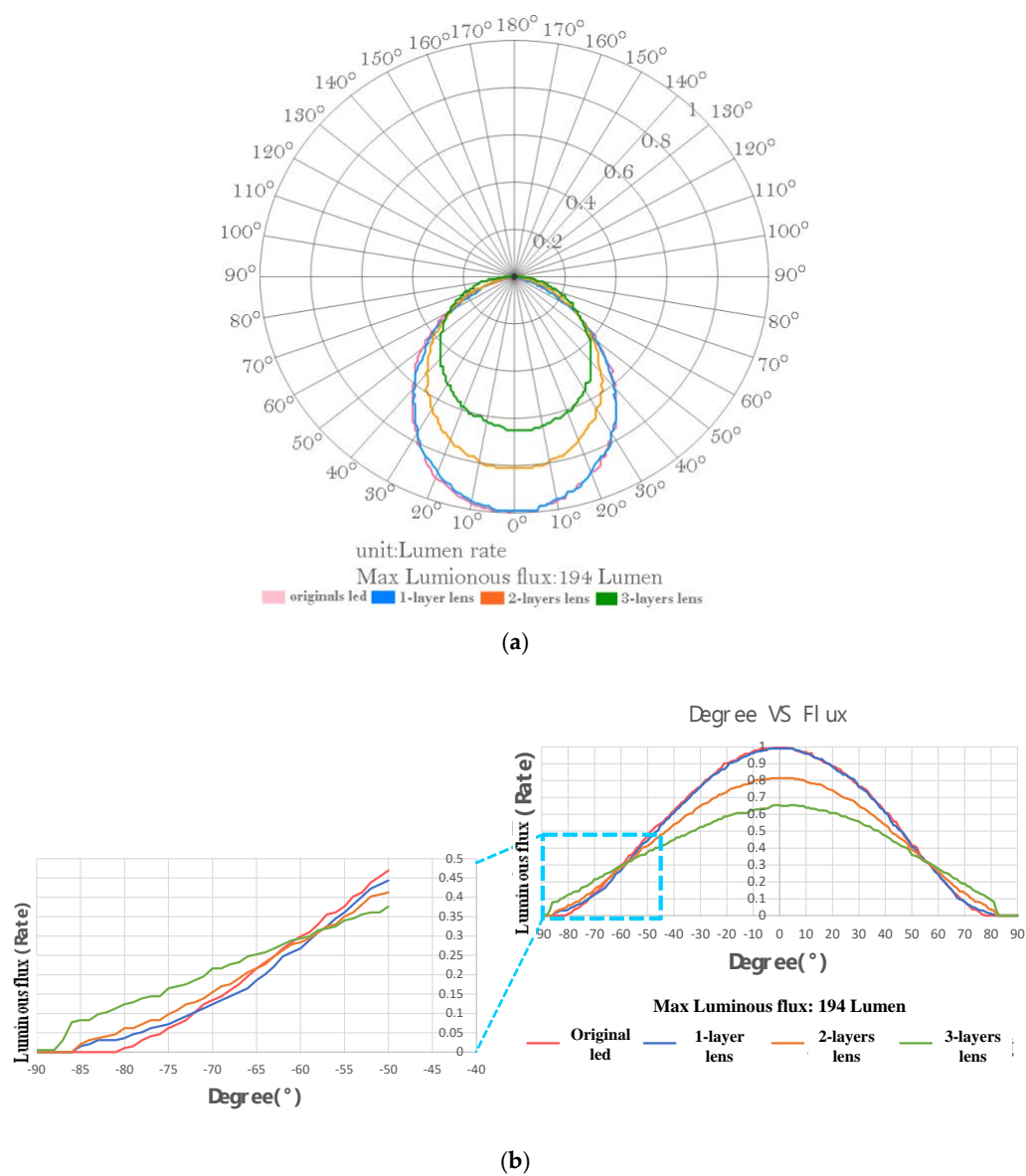


Figure 18. Relationship between LED lens rotation angle and luminous flux (1 is equal to 194 lumen, 0.8 is equal to 0.8×194 lumen, etc.). (a) Polar plot. (b) Cartesian graph.

Table 1. Spectrometer measurements data of the LED lens.

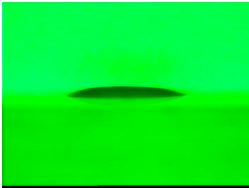
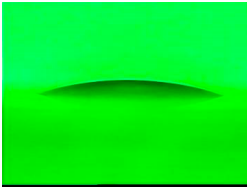
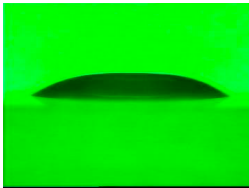
Layers	0	1	2	3
CIE 1931_x	0.321554	0.307743	0.302103	0.291521
CIE 1931_y	0.350373	0.318445	0.308519	0.291586
CCT	5966	6890	7407	8724
CRI	68	68	68	68
LUX	150	144	121	102

Figure 18a, shows that the luminous flux of a single-layer lens LED was greater than that of a no LED lens when the LED lens rotation angle was more than -73° and 72° ; the two-layer lens had a significantly higher luminous flux when the LED lens rotation angle was more than -64° and 58° ; and the luminous flux of a three-layer lens was more pronounced when the LED lens rotation angle was more than -61° and 57° . Figure 18b, a cartesian graph, can more clearly show the various phenomena as described in Figure 18a. From Figure 18a,b, it can be seen that if the layers of n increase, the luminous flux of the high rotation angle will be improved.

4.2. Lens Array Applied to Solar Cells

Since the lens array focuses sunlight, it can enhance the intensity of solar radiation emitted using the solar cell. It can also indirectly reduce the reflection of sunlight and increase the possibility of secondary reflection. Figure 19a shows a dispensing path with spacing distance x (mm) of the n -th layer. As shown in Figure 19b, a UV fluid of CP2000 viscosity was dispensed on the glass at spacing distances of $x = 1$ mm (x_1), $x = 1.5$ mm ($x_{1.5}$) and $x = 2$ mm (x_2) to form a lens array as a solar cells mask (shown in Figure 19c), and the tooling was controlled at a temperature of 30°C . The lens was stacked for n layers to increase its height and the contact angle. After curing, an image measuring instrument was used to observe and measure its surface contact angle $\theta_c(^{\circ})$, width, and height, etc. Table 2 shows the lens shape and size values of different layers ($n = 3, 10$ and 15) but the same spacing distance ($x = 2$ mm); the measurement system of the maximum power of the solar cell for different rotation angles is shown in Figure 20. Figure 21 shows the relationship between the rotation angle and its maximum power for solar cells with different lenses. The top and side view of the three different spacing distances ($x = 1$ mm, 1.5 mm, and 2 mm) all with the same thickness ($n = 3$) of lens array are shown in Table 3.

Table 2. The lens shape and the data of lens sizes.

Lens Shape			
			
Layers n	3	10	15
x (mm)	2	2	2
Lens height (μm)	57.0	105.7	147.7
Lens width (μm)	936.7	1255.3	1457.3
Contact angle $\theta_c(^{\circ})$	13.9	19.1	22.9

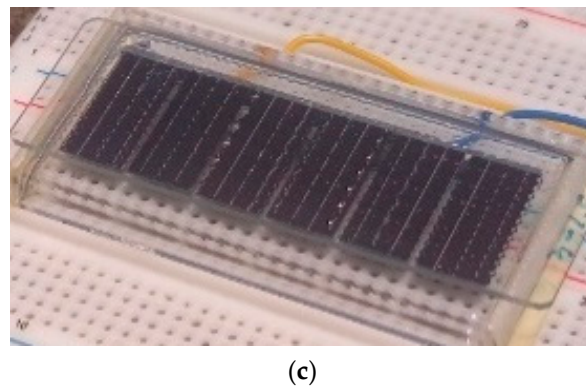
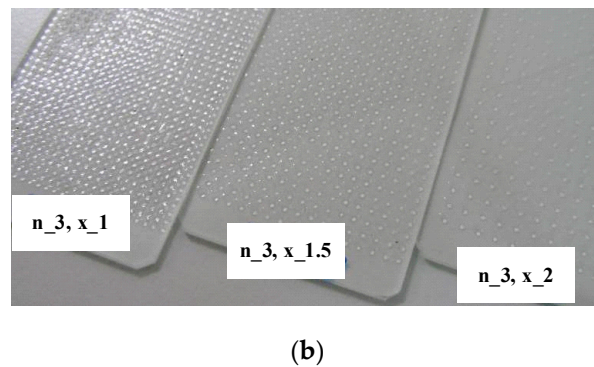
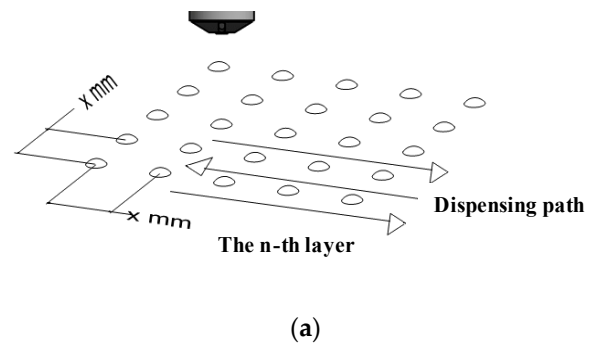


Figure 19. (a) Lens array spacing distance x (mm) and dispensing path. (b) Lens array dispensed on the glass as a mask (n : Layer; x : Spacing distance (mm)). (c) Glass lens array applied to mask solar cells.

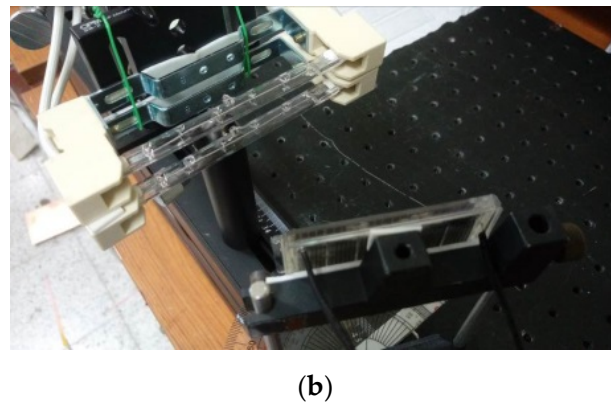
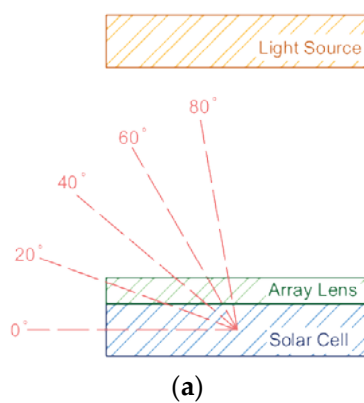


Figure 20. 24 h simulated measurement system with solar cell rotation 10° per 45 min. (a) The schematic diagram. (b) The actual devices used.

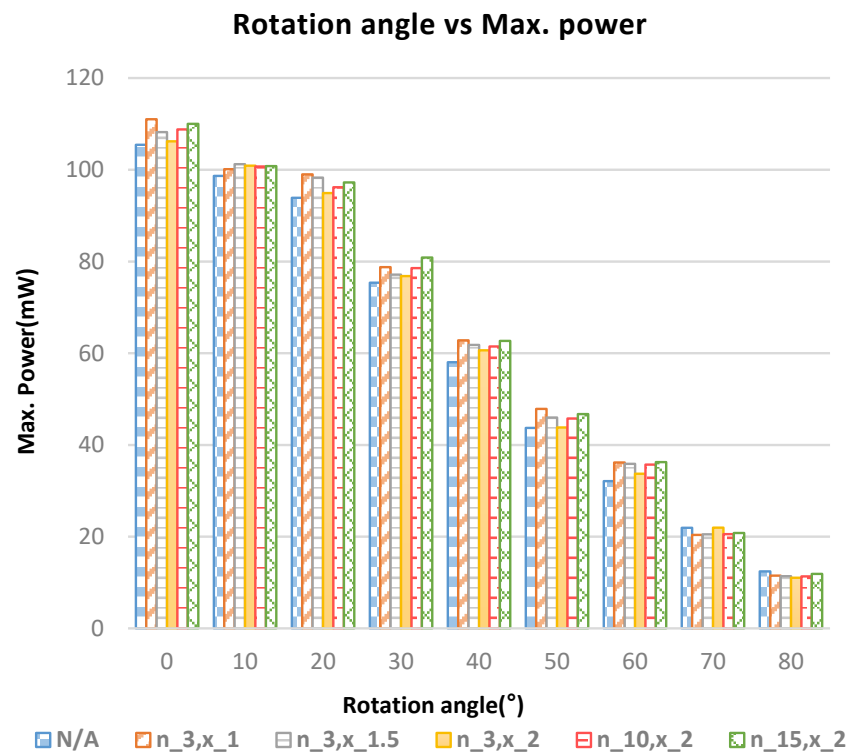
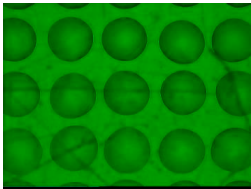
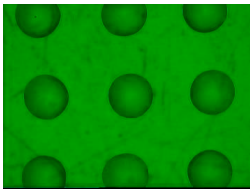
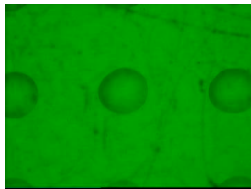
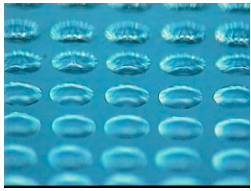
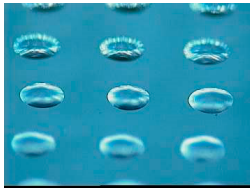
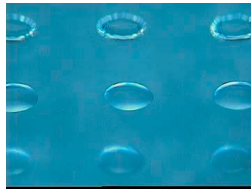


Figure 21. The relationship between the solar cell rotation angle and maximum power of different lenses (n: Layer; x: Spacing distance mm).

Table 3. The top view and side view of different lens array spacing distance (n: Layer; x: Spacing distance (mm)).

		n = 3		
		x = 1 mm	x = 1.5 mm	x = 2 mm
Top view				
Side view				

During summer in Taipei, the earth takes about 45 min to turn 10 degrees. These data were used to simulate a full-day of solar cell power generation in Taipei with different lenses, as listed in Table 4. In Table 4, we can see that, when using the same number of layers on the solar cell lens array cell, increasing the spacing distance reduced the amount of power generated over a 24-h period. Furthermore, increasing the layers increased the power generation.

Table 4. Different lens arrays used in the simulated full-day solar cell power generation for Taipei (in $n = 3$, and $x = 2$ mm).

Lens	N/A	n_3, x_1	n_3, x_1.5	n_3, x_2	n_10, x_2	n_15, x_2
power generation (mW-hr)	812.25	851.37	840.49	824.98	838.66	850.86
Percentage of raise (%)	-	4.82	3.48	1.57	3.25	4.75

5. Conclusions

From the experiment, we can see that UV fluids with different viscosities create different contact angles under the same conditions. The higher the viscosity, the greater the contact angle. The tool temperature affects the surface tension of the fluid. As the tool temperature rises, the contact angle decreases. In this study, we controlled the contact angle of lenses by controlling the fluid viscosity and the tool temperature.

By dispensing UV fluid onto a packaged LED product to form the LED lens, we found that the luminous flux of a single-layer LED lens was greater than that of no LED lens when the LED lens rotation angle was greater than -73° and 72° ; the two-layer lens LED had a luminous flux improvement when the LED lens rotation angle was greater than -64° and 58° , and the luminous flux increase in a three-layer lens LED was most obvious when the LED lens rotation angle was greater than -61° and 57° .

As the second experiment shows, by dispensing UV fluid onto a glass to form glass lens array and mask it on a solar cell to measure its maximum power generated, we found that the highest efficiency was achieved in densely spaced or highly stacked lens arrays. A simulation of a 24-h period of power generation by a solar cell located in Taipei showed that the higher the lens array layer, the higher the power generation will be. The comparison of different lens arrays is shown in Table 4 with a layer of $n = 3$ vs different spacing distance ($x = 1$ mm, 1.5 mm, 2 mm) and a spacing distance of $x = 2$ mm vs different layers ($n = 3, 10, 15$). This was also true on the same condition of lens array spacing distance of $x = 2$ mm. The most significant finding was that the full-day power generation for a no lens array of solar cell was about 812.25 mW-hr, while a 15-layer lens array solar cell had the highest output of 850.86 mW-hr—an overall increase of about 4.75% compared to a no lens solar cell. It is the increased layers of the lens that caused the contact angle to be increased (as shown in Table 2) and focus sunlight more to increase solar cell radiation intensity. Furthermore, as seen in Table 4, on the same condition of lens array layers of $n = 3$, increasing spacing distance reduced power generation. Lastly, we found the full-day power generation of a 1 mm spaced lens array solar cell was about 851.37 mW-hr—an overall increase of around 4.82% when compared to a no lens solar cell.

Author Contributions: Proposed the main idea and performed the investigation, F.-M.Y. and K.-W.J.; Developed the software, C.-T.T.; Wrote and revised the whole manuscript, F.-M.Y.; Lead the project, F.-M.Y. and R.-S.C.

Funding: This research was funded by the Ministry of Science and Technology, Taiwan, R.O.C., under Contract MOST108-2637-E-129-002.

Conflicts of Interest: The authors declare no conflict of interest.

References

1. Furlan, W.D.; Ferrando, V.; Monsoriu, J.A.; Zagrajek, P.; Czerwinska, E.; Szustakowski, M. 3D printed diffractive terahertz lenses. *Opt. Lett.* **2016**, *41*, 1748–1751. [CrossRef] [PubMed]
2. Zhang, S.; Arya, R.K.; Pandey, S.; Vardaxoglou, Y.; Whittow, W.; Mittra, R. 3D-printed planar graded index lenses. *IET Microw. Antennas Propag.* **2016**, *13*, 1411–1419. [CrossRef]
3. MacFarlane, D.L.; Narayan, V.; Tatum, J.A.; Cox, W.R.; Chen, T.; Hayes, D.J. Microjet Fabrication of Microlens Arrays. *IEEE Photonics Technol. Lett.* **1994**, *6*, 1112–1114. [CrossRef]
4. Luxexcel, 3D Printed Optics. Available online: <https://www.luxexcel.com/> (accessed on 26 June 2017).
5. McMahon, T.; Bonner, J.T. *On Size and Life, Scientific*; Holt & Company: Kosciusko, MS, USA, 1983.

6. Young, T. An Essay on the Cohesion of Fluids. *Philos. Trans. R. Soc. Lond.* **1805**, *95*, 65–87. [[CrossRef](#)]
7. Romi, S.; David, A.; Bruno, B.; Gorman, C.B.; Biebuyck, H.A.; Whitesides, G.M. Control of the Shape of Liquid Lenses on a Modified Gold Surface using an Applied Electrical Potential Across a Self-Assembled Monolayer. *Langmuir* **1995**, *11*, 2242–2246.
8. Asymtek. *Dispensing System Installation and Service Manual*; Asymtek: Carlsbad, CA, USA, 2002; pp. 20–45.
9. Asymtek. *Fluidmove for Windows XP®Version 5.0 User Guide*; Asymtek: Carlsbad, CA, USA, 2005; pp. 4–25.
10. Mahajan, V.N. *Fundamentals of Geometrical Optics*; SPIE Press: Bellingham, WA, USA, 2014.



© 2019 by the authors. Licensee MDPI, Basel, Switzerland. This article is an open access article distributed under the terms and conditions of the Creative Commons Attribution (CC BY) license (<http://creativecommons.org/licenses/by/4.0/>).